Surface Wave Effects on the Wind-Power Input to Mixed Layer Near-inertial Motions

Article *in* Journal of Physical Oceanography · March 2017

DOI: 10.1175/JPO-D-16-0198.1

Guoqiang Liu
Bedford Institute of Oceanography

W. Perrie
Bedford Institute of Oceanography, Fisheries…

The DOI for this manuscript is doi: 10.1175/JPO-D-16-0198.1

The final published version of this manuscript will replace the preliminary version at the above DOI once it is available.

If you would like to cite this EOR in a separate work, please use the following full citation:

Liu, G., W. Perrie, and C. Hughes, 2017: Surface Wave Effects on the Wind-Power Input to Mixed Layer Near-inertial Motions. J. Phys. Oceanogr. doi:10.1175/JPO-D-16-0198.1, in press.

Surface Wave Effects on the Wind-Power Input to Mixed Layer Near-inertial Motions

Guoqiang Liu[1,2,3,4*], William Perrie[3,4] and Colin Hughes[3,4]

[1]School of Marine Sciences, Nanjing University of Information Science and Technology, Nanjing, Jiangsu, China

[2]Jiangsu Research Center for Ocean Survey and Technology, Nanjing, Jiangsu, China

[3]Department of Engineering Mathematics and Internetworking Dalhousie University, Halifax, Nova Scotia, Canada

[4]Bedford Institute of Oceanography, Fisheries and Oceans Canada, Dartmouth, NS, Canada

Re-submitted to Journal of Physical Oceanography

*Corresponding Author:
Guoqiang Liu
Bedford Institute of Oceanography, 1 Challenger Dr., Dartmouth, Nova Scotia B2Y 4A2 Canada
Email: Guoqiang.Liu@dfo-mpo.gc.ca
Phone 902 426 3147

Abstract

Ocean surface waves play an essential role in a number of processes that modulate the momentum fluxes through air-sea interface. In this study, the effects of evolving surface waves on the wind power input (WPI) to near inertial motions (NIMs) are examined by using momentum fluxes from a spectral wave model and a simple slab ocean mixed layer model. Single-point numerical experiments show that, without waves, the WPI and the near-inertial kinetic energy (NI-KE) are overestimated by about 20% and 40%, respectively. Globally, the overestimate in WPI is about 10% during 2005-2008. The largest surface wave effects occur in the winter storm track regions in the mid-latitude northwestern Atlantic, Pacific and in the Southern Ocean, corresponding to large inverse wave age and rapidly varying strong winds. A relatively low frequency of occurrence of wind sea is found in the mid-latitudes, which implies that the influence of evolving surface waves on WPI is intermittent, occurring less than 10% of the total time, but making up the dominant contributions to reductions in WPI. Given the vital role of NIMs in diapycnal mixing at the base of the mixed layer and the deep ocean, the present study suggests that it is necessary to include the effects of surface waves on the momentum flux, for example in studies of coupled ocean-atmosphere dynamics, or climate models.

1. Introduction

Ocean surface waves and near inertial motions (NIMs) are typically generated by winds over the ocean surface, transferring momentum and energy from the atmosphere to the ocean, mostly through resonant interactions. Specifically, surface waves are generated via the resonance between the wind pressure perturbations and initial capillary waves on the ocean surface, which are amplified and grow (e.g., Miles 1957, 1962; 1965; Phillips 1957; Belcher and Hunt 1993; Janssen 2004). By comparison, NIMs are generated and amplified in the oceanic mixed layer by near inertial wind fluctuations mainly from winter storms (e.g., D'Asaro 1985; 1995).

Near inertial motions are ubiquitous in the upper ocean. In the open oceans, near inertial waves (NIWs) are excited by convergences and divergences of near inertial motions in the mixed layer. The NIWs are the dominant mode of the high-frequency variability of ocean processes (e.g., Kunze 1985; Ferrari and Wunsch 2009; Alford 2016). They are thought to be a source of abyssal diapycnal mixing which drives the meridional overturning circulation and maintains the abyssal stratification (Munk and Wunsch 1998; Wunsch and Ferrari 2004; Jing and Wu 2014; Alford et al. 2016). In addition, because of the strong associated shear variance, NIMs play a significant role in setting the depth of the ocean mixed layer (e.g., Jochum et al. 2013). By accounting for the effects of NIMs in a climate model, it is found that NIMs can have a potential global impact on the atmospheric circulation by teleconnections that influence the sea surface temperature, especially in the tropics (Jochum et al. 2013). Therefore, given the potential role of NIMs in the upper ocean, deep ocean and thus, the global climate system, knowledge about the magnitude and spatiotemporal patterns of wind power input (WPI) into NIMs in the oceanic mixed layer is of vital importance and is being extensively analyzed. Recent estimates of WPI have included applications of simple slab ocean models, as well as more sophisticated general circulation models (Alford 2001, 2003; Furuichi et al. 2008; Zhai et al. 2005, 2007, 2009; Rath et al. 2013, 2014; Rimac et al. 2013; 2016).

Typically, no matter which model is applied, the wind stress parameterization is the most critical factor, determining most of the uncertainties in WPI and NIMs (e.g., Alford 2001). Generally, accurate estimates of WPI are sensitive to the temporal and spatial resolutions of surface wind stress (e.g., Klein et al. 2004; Jiang et al. 2005; Rimac et al. 2013). As well, it has been reported that a large reduction of about 40% of the estimated NI-KE for the Southern Ocean occurs when the ocean surface velocity is included in the wind stress parameterization (Rath et al. 2013). Besides, in most ocean general circulation models (OGCMs), estimates of WPI are reduced owing to the linear temporal and bilinear or bicubic spatial interpolation methods used for wind stress (Jing et al. 2015; 2016). However, when estimating WPI, these studies overlook an important process, that is, the development of surface waves (sea-state), which are capable of influencing the momentum flux from the atmosphere to the ocean. Generally, the main contributions to WPI occur when moving storms generate high winds as they pass over the ocean (e.g., D'Asaro 1985; Wunsch and Ferrari

2004). As storms go from generation, to growth and development, and finally to dissipation, they are also drivers for associated surface waves.

Surface waves, as the most visible oceanic phenomenon, on one hand, directly affecting the ocean surface boundary layer (OSBL), sea surface temperature and vertical mixing through wave breaking, Langmuir turbulence and non-breaking wave induced turbulence (e.g., Craig and Banner, 1994; Craig 1996; Polton and Belcher 2007; McWilliams et al. 2012; Qiao et al., 2004; Fan and Griffies 2014). On the other hand, surface waves indirectly affect the upper ocean dynamics by modifying the momentum fluxes injected into the ocean column. Specifically, the wind forcing on the surface waves, defined as air-side stress $\boldsymbol{\tau}_{\mathbf{a}}$ and the exact momentum forcing causing the generation of currents, like NIMs, in the ocean column, defined as water-side stress $\boldsymbol{\tau}_{\mathbf{oc}}$ are dependent on the surface wave evolution (e.g., Janssen 2004; Janssen 2012; Breivik et al. 2015).

On the air side, the presence of surface waves determines the oceanic surface roughness felt by the airflow, which modulates the drag coefficient (e.g., Donelan et al. 1993; 1995; Liu et al. 2011; 2013) and therefore determines $\boldsymbol{\tau}_{\mathbf{a}}$. On the water side, when air-side stress $\boldsymbol{\tau}_{\mathbf{a}}$ forces the ocean boundary layer, it is felt firstly by the surface waves. During their growing stage, surface waves absorb and store energy and momentum from the wind which are released when the surface waves break (e.g., Ardhuin et al., 2004; Janssen 2004; Rascle et al. 2006; Ardhuin and Jenkins 2006; Janssen 2012). These wave-related processes decrease (or increase) the water-side stress $\boldsymbol{\tau}_{\mathbf{oc}}$ relative to the air-side stress $\boldsymbol{\tau}_{\mathbf{a}}$, depending on whether surface waves are growing or decaying.

Currently, all the estimates of WPI implicitly assume $\boldsymbol{\tau}_{\mathbf{a}} = \boldsymbol{\tau}_{\mathbf{oc}}$, which means that there is no net momentum gain or loss due to surface waves. This assumption results in large biases in regions dominated by growing surface waves in the open oceans, for example the mid-latitude storm track areas (e.g., Chen et al., 2002; Hanley et al. 2010). Typically, $\boldsymbol{\tau}_{\mathbf{a}} = \boldsymbol{\tau}_{\mathbf{oc}}$ happens only when the surface waves are in equilibrium, with the energy injected by the wind in balance with wave dissipation. However, this case rarely happens through the analysis of global wave data generated by spectral wave models (e.g., Hanley et al. 2010).

The main objective of this paper is to estimate and qualify the influence of surface wave evolution on WPI and to examine the geographical variation of this effect over the global oceans during years from 2005 to 2008. Typically, under extreme conditions, like hurricanes/storms, momentum flux is reduced by as much as 10% locally around the hurricane/storm center and advected away due to surface waves (e.g., Ardhuin et al., 2004; Janssen 2012). This is especially the case during fast moving storms, when the reduction of momentum flux to the ocean can reach 25% (Fan et al. 2010). Thus, a certain portion of momentum is effectively stored in the ocean surface wave field during their growing stage. Concomitantly, with the passage of hurricanes/storms, most of the NIMs are generated and the greatest WPI occurs (e.g., D'Asaro 1985, Wunsch and Ferrari 2004), often corresponding to the growing stage of the surface waves (e.g., Hwang 2016). Thus, the evolution of surface waves exerts significant effects on NIMs and thus on WPI in ocean areas having high winds and rapid storm variability.

The paper is organized as follows. Section 2 describes the momentum fluxes $\boldsymbol{\tau}_{\mathbf{a}}$ and $\boldsymbol{\tau}_{\mathbf{oc}}$ generated by a modern operational wave model and near inertial currents generated by a simple slab model. A single-point numerical experiment is described, with time series analysis of the effects of surface waves on WPI and NI-KE. Section 3 describes the spatial distribution of seasonally averaged WPI, inverse wave age and the frequency of occurrence of wind sea and swell regimes. The spatial relationship between WPI, inverse wave age and associated parameters over different ocean basins is also presented. Discussion and Conclusions are given in Section 4.

2. Data and Methods

2.1 Surface wave effects on near inertial motions

Surface waves can directly influence slowly evolving long waves, such as infragravity waves, as well as ocean currents including near inertial currents. There are six major processes dominating the impacts of surface waves in the upper ocean dynamics: wave breaking; Langmuir turbulence; non-breaking wave induced turbulence; Coriolis-Stokes force represented as $-\mathbf{f} \times \mathbf{U_s}$ where $\mathbf{f}$ is the Coriolis parameter and $\mathbf{U_s}$ is the Stokes drift; radiation stress or the equivalent vortex force plus the Bernoulli head gradient (McWilliams 2004); and 6) water-side stress $\boldsymbol{\tau}_{\mathbf{oc}}$

with its dependence on sea-state. Among these, wave breaking plays an important role in enhancing turbulence in the uppermost ocean. Langmuir turbulence and non-breaking wave induced turbulence are believed to significantly elevate the mixing level intensity and to possibly deepen the mixed layer depth in the upper ocean (*e.g.*, Craig and Banner 1994; Qiao et al. 2004; McWilliams et al. 1997; 2012; Wu et al. 2015).

The mixed layer depth is a critical parameter for calculating the WPI. Here, we use the monthly climatological mixed layer depth in the slab model, computed as the shallowest occurrence of potential density bigger than 0.125 kg/m^3 (Monterey and Levitus (1997). The monthly climatological mixed layer is implicitly assumed to include the effects of wave breaking, Langmuir turbulence and non-breaking wave induced turbulence. The Stokes-Coriolis force and radiation stress represent additional forces due to the presence of surface waves. Although both can directly drive the near inertial currents (Hasselmann 1970), the investigation of near inertial motions driven by processes associated with surface waves is beyond the range of this paper and will be discussed elsewhere. In this paper, we focus on the effects of sea-state evolution on the water-side stress $\boldsymbol{\tau}_{\mathbf{oc}}$ and thus on estimating WPI over the global oceans. As shown in the following sections, because of the presence of growing surface waves, the momentum lost from the atmosphere is partially stored in surface waves, and therefore cannot immediately provide the forcing for the Eulerian currents. This result is especially evident for strong rapidly varying wind events like hurricanes and storms, where most of the WPI occurs.

2.2 Air-side stress $\boldsymbol{\tau}_{\mathbf{a}}$ and water-side stress $\boldsymbol{\tau}_{\mathbf{oc}}$

In order to account for the effect of the evolution of surface waves in modulating the water-side stress $\boldsymbol{\tau}_{\mathbf{oc}}$, a third-generation spectral wave model, WAVEWATCH-III, is used to obtain the momentum flux from the atmosphere to surface waves (Rascle et al. 2008; Rascle and Ardhuin 2013). Typically, a spectral wave model (Tolman 2002; 2014) solves the spectral balance equation (Komen et al. 1994) to give the two-dimensional wave energy spectrum $E(\omega,\theta)$, as a function of angular frequency ω and direction θ, according to the equation,

$$\frac{\partial E}{\partial t} + \frac{\partial}{\partial x} \cdot \left(\mathbf{c_g} E(\omega,\theta)\right) = S_{in} + S_{nl} + S_{diss} \tag{1}$$

where $\mathbf{c_g}$ is the wave group velocity. Here, the terms on the right side are the source terms which represent the wind input to surface waves (S_{in}), the nonlinear wave-wave interactions (S_{nl}), and wave dissipation (S_{diss}) (e.g., Komen et al. 1994). Based on the wave spectrum, the total wave momentum $\mathbf{P}$ is defined as

$$\mathbf{P} = \rho_w g \int_0^{2\pi} \int_0^{\infty} \frac{\mathbf{k}}{\omega} E(\omega,\theta) d\omega d\theta, \tag{2}$$

where ρ_w is density of sea water, g is the gravity acceleration and $\mathbf{k}$ is the wavenumber vector. It follows from equation (2) that the momentum fluxes to, and from, the wave field are given by the rate of change of wave momentum in time. One may distinguish different momentum fluxes depending on the different physical processes. Combining (1) and (2), the wave induced stress, representing the momentum flux from the atmosphere to waves, is given by

$$\boldsymbol{\tau}_{\mathbf{in}} = \rho_w g \int_0^{2\pi} \int_0^{\infty} \frac{\mathbf{k}}{\omega} S_{in}(\omega, \theta) d\omega d\theta \qquad (3)$$

where S_{in} describes the generation and growth of surface waves forced by the air-side stress $\boldsymbol{\tau}_{\mathbf{a}}$ and therefore represents the momentum and energy transfer from the atmosphere to ocean surface waves. While the wave dissipation stress is given by

$$\boldsymbol{\tau}_{\mathbf{diss}} = \rho_w g \int_0^{2\pi} \int_0^{\infty} \frac{\mathbf{k}}{\omega} S_{diss}(\omega, \theta) d\omega d\theta \, , \qquad (4)$$

where S_{diss} describes the dissipation of waves by processes such as white-capping, large scale breaking and eddy-induced damping and bottom friction. It is important to note from equations (2) - (4) that the momentum flux is mainly determined by the high frequency region of the wave spectrum, whereas to some extent, the energy flux is determined by the low frequency waves, e.g., swell. Therefore, the water-side stress $\boldsymbol{\tau}_{\mathbf{oc}}$, representing the momentum flux to the oceanic column, can be represented as the sum of the flux transferred by turbulence across the air-sea interface, $\boldsymbol{\tau}_{\mathbf{a}} - \boldsymbol{\tau}_{\mathbf{in}}$ and the momentum flux transferred from the waves into the currents due to wave breaking, $\boldsymbol{\tau}_{\mathbf{diss}}$,

$$\boldsymbol{\tau}_{\mathbf{oc}} = \boldsymbol{\tau}_{\mathbf{a}} - \rho_w g \int_0^{2\pi} \int_0^{\infty} \frac{\mathbf{k}}{\omega} (S_{in} - S_{diss}) d\omega d\theta \,. \qquad (5)$$

Therefore, in rapidly varying circumstances over the open ocean, such as explosively developing storms, the fluxes are dependent on the surface wave development. In the coastal areas, the fetch also affects the momentum stored in the wave field (Mitsuyasu 1985; Ardhuin et al., 2004). Note that most of the momentum flux $\boldsymbol{\tau}_{\mathbf{a}}$ from the atmosphere to the ocean transits through the wave field. With the exception of very low winds (less than 2.5 m/s), only a small fraction of $\boldsymbol{\tau}_{\mathbf{a}}$, goes directly from the atmosphere to the ocean via the mean viscous stress at the surface, which can be represented as $\boldsymbol{\tau}_{\mathbf{a}} - \boldsymbol{\tau}_{\mathbf{in}}$ (Dobson 1971; Snyder et al. 1981; Donelan 1998).

In this present study, $\boldsymbol{\tau}_{\mathbf{a}}$ and $\boldsymbol{\tau}_{\mathbf{oc}}$ are provided by the well-validated IOWAGA (Integrated Ocean Waves for Geophysical and Other Applications) global wave hindcast, constructed by WAVEWATCH-III wave model (Tolman 2014), using newly developed parameterizations for wave generation (S_{in}) and explicit swell dissipation (S_{diss}) source terms, which are the most important source terms for estimating the momentum fluxes (Ardhuin et al. 2010; Rascle and Ardhuin 2013). The IOWAGA wave hindcast was constructed by using winds from the Climate Forecast

System Reanalysis (CFSR) data set (Saha et al. 2010). The spatial grid resolution is 0.5° by 0.5° covering the entire ocean. The wave spectra were discretized by using 32 frequencies exponentially spaced from 0.038 Hz to 0.72 Hz so that the bandwidth between two successive frequencies f_i and f_{i+1} is 0.10 f_i, with a constant 15° angular discretization given by 24 angular directions.

The momentum flux from waves to ocean currents, denoted as the water-side stress $\boldsymbol{\tau}_{\mathbf{oc}}$, involves solely the sum of the source functions of the spectral wave energy equation and therefore only involves the total rate of change of wave momentum. In addition, the first moment of the wave energy spectrum, *e.g*., the wave mean period, is directly connected to wave momentum (e.g., Holthuijsen 2007; Janssen 2012). Therefore, it follows that any wave model that produces accurate mean wave periods in comparison with buoy measurements will also produce reliable estimates of the momentum flux from waves to the ocean. Hence, although it may be difficult to directly validate air–sea energy and momentum exchanges with observations, the data applied here can be regarded as reliable, based on the high correlations of the IOWAGA data (*e.g*. wave heights, mean wave periods) with global wave measurements from altimeters, buoys and synthetic aperture radar (SAR) (Rascle et al. 2008; Rascle and Ardhuin, 2013).

2.3 Estimating WPI with slab model

Generally, because observations of winds and surface currents, at high frequency in time and high spatial resolution, are not available over open oceans, estimates of WPI mainly depend on two modeling approaches. In one approach, high-frequency and high-resolution winds are used to directly drive a primitive equation ocean model to obtain near inertial motions and thereby determine WPI. The calculation of WPI is often completed by taking the dot product of the near inertial current $\mathbf{U_I}$ and the wind stress at the near inertial frequency band $\boldsymbol{\tau}_\mathbf{I}$ as,

$$W = \boldsymbol{\tau}_\mathbf{I} \cdot \mathbf{U_I}. \tag{6}$$

In the other approach, used in the present study, a simple damped slab mixed layer model (hereafter denoted the slab model), is used to describe the temporal evolution of inertial oscillations in a one-dimensional mixed layer of constant depth, as a balance between wind forcing and a parameterized (linear) damping. The slab model applied here follows the formulation proposed by Alford (2003). The equations for the velocity components (u and v) of the oceanic mixed layer (D'Asaro 1985) are given as,

$$\frac{\partial Z}{\partial t} + (r + i \cdot f)Z = \frac{T}{H} \tag{7}$$

where $Z = u + i \cdot v$ represents the mixed layer current in terms of complex quantities and H is the mixed layer depth. In the present study, H is obtained from the monthly climatology of Monterey and Levitus (1997), T is the wind stress represented as complex form and r is the frequency dependent damping parameter, often written as $r = r_o(1 - e^{-\sigma^2/2\sigma_c^2})$, where σ represents the angular frequency, $r_o = 0.15f$ and $\sigma_c = f/2$. Physically, the damping parameter r represents the energy loss through shear instabilities at the base of the mixed layer (Crawford and Large 1996; Skyllingstad et al. 2000), as well as through the radiation of near-inertial internal waves into the deep ocean. Taking the Fourier transform of equation (7) leads to a spectral solution,

$$\hat{Z}(\sigma) = \frac{\hat{T}(\sigma)}{H}\frac{r - i(f+\sigma)}{r^2 + (f+\sigma)^2}, \tag{8}$$

where $\hat{T}(\sigma)$ is the wind stress in Fourier space. Therefore, $Z(t)$ can be obtained by inverting the Fourier transform of $\hat{Z}(\sigma)$, which may be represented as the sum of the Ekman current, $Z_E(t)$ and the near-inertial current, $Z_I(t) = u_i(t) + i \cdot v_i(t)$,

$$Z(t) = Z_E(t) + Z_I(t). \tag{9}$$

Combining equations (7)-(9), estimates for NI-KE and WPI may be given as, respectively,

$$\text{NI-KE}=\frac{1}{2}(u_i^2(t)+v_i^2(t)) \quad (10)$$

and

$$\pi = -\rho_w H \Re[\frac{Z_I^*}{\omega}\frac{d}{dt}(\frac{T}{H})]. \quad (11)$$

Following the heuristic arguments by Alford (2003), a simplified approximation to equation (11) is made, representing the dot product of the wind stress vector and the mixed layer inertial currents in complex form as,

$$\pi = Re(\rho_w \cdot Z \cdot T^*) \quad (12)$$

where π represents WPI, and $*$ denotes the complex conjugate.

We note that the slab model has inherent errors, in terms of its ability to calculate the near inertial current, and hence, to estimate WPI. These inherent errors include: (a) the finite temporal and spatial resolutions of winds, and (b), overestimates due to inadequacies and approximations in the slab model, *e.g.*, lacking the processes related to shearing at the base of mixed layer (Plueddemann and Farrar 2006; Alford and Whitmont 2007; Furuichi et al 2008). Therefore, for these reasons, significant underestimates in WPI may occur. Despite these uncertainties, the estimated order of magnitude for WPI has been shown to still be reliable (*e.g.*, Alford 2001; Alford 2003). Moreover, we are only concerned with WPI estimates as determined by the slab model resulting solely with variations in wind stress forcing for the air-side stress $\boldsymbol{\tau_a}$ and water-side stress $\boldsymbol{\tau_{oc}}$. Therefore, biases in the slab model are not expected to qualitatively alter our conclusions.

2.4 Single-Point WPI and NI-KE estimates for a sudden wind change event

In this section, surface wave effects on WPI and NI-KE are examined, based on the slab model with specified mixed layer depth, forced by a sudden wind event with the varying momentum fluxes ($\boldsymbol{\tau_a}$ and $\boldsymbol{\tau_{oc}}$). Generally, under the conditions of wind-wave equilibrium (or fully developed seas), the deviation between $\boldsymbol{\tau_a}$ and $\boldsymbol{\tau_{oc}}$ will vanish. However, this is rarely the case. Usually, the surface waves are fetch– and duration–limited and winds are rarely constant long enough for seas to become fully developed (*e.g.*, Hasselmann et al., 1973; Perrie and Toulany, 1990; Chen et al. 2002; Drennan et al. 2003). It is known that the wind sea is prevalent in the mid-latitude storm track regions while swell tends to be dominant in the tropics (Hanley et al. 2010). These characteristics of surface waves may be assessed based on the values of inverse wave age $1/\beta$, defined as,

$$1/\beta = {}^{U_{10} cos\theta_w}/_{c_p}. \tag{13}$$

The inverse wave age is believed to be a useful indicator of the degree of coupling between the wind and waves and in distinguishing different wave regimes (*e.g.*, Hanley et al. 2010). Here, U_{10} is the wind speed at 10 m above sea level, c_p is the peak phase speed and θ_w is the relative angle between the wind and waves.

Following Alves et al. (2003), when $1/\beta > 0.83$, the waves are able to grow by absorbing and storing momentum from winds. During the growing stage, wind–generated waves are dominant and typically $|\boldsymbol{\tau}_{\mathbf{a}}| > |\boldsymbol{\tau}_{\mathbf{oc}}|$. The intermediate range, when $0.15 < 1/\beta < 0.83$, corresponds to the mixed wind sea–swell sea state, composed of both wind sea and swell. This range consists of both growing waves extracting momentum from the wind, as well as fast waves (swell) imparting momentum back to the wind. Finally, $1/\beta < 0.15$ corresponds to the swell-dominated stage, in which the sea state is dominated by long-wavelength swell and the momentum flux sometimes experiences sign reversal, which may lead to the situation where $|\boldsymbol{\tau}_{\mathbf{a}}| < |\boldsymbol{\tau}_{\mathbf{oc}}|$. Note that growing waves may still extract momentum from winds in this range. However, these are only qualitative descriptions to characterize different sea states and the corresponding status of the air-sea momentum flux, rather than hard limits.

As a test case, we consider the effects of the waves on the momentum flux and on WPI in the case of a sudden change in the wind direction and speed, with the mixed layer depth setup as *H* = 50 m at this single point. Specifically, in Fig. 1, we present 4 days (day 7.5 to day 12.5) time series of the difference in magnitudes between the air-side stress $\boldsymbol{\tau}_{\mathbf{a}}$ and water-side stress $\boldsymbol{\tau}_{\mathbf{oc}}$ ($\Delta\tau = |\boldsymbol{\tau}_{\mathbf{a}}|$-$|\boldsymbol{\tau}_{\mathbf{oc}}|$), and inverse wave age $1/\beta$, during January 2005 at the location [57°, -15°] in the North Atlantic Ocean. In this case, the most notable sudden wind change lasts approximately from day 10.2 to day 12; the wind increases sharply from about 6 to 30 m/s, followed by a drop to 5 m/s and a change in wind direction by about 90^{o} from north to the east. On day 10.2, the inverse wave age is small, $1/\beta = 0.04$, and the corresponding ratio Ra between $\Delta\tau$ and $|\boldsymbol{\tau}_{\mathbf{oc}}|$ is only -10.5%, indicating that under swell–dominated conditions, the magnitude of $\boldsymbol{\tau}_{\mathbf{oc}}$ is larger than that of $\boldsymbol{\tau}_{\mathbf{a}}$. With the sharp wind speed increase beginning at day 10.2, a young wind wave regime begins to be generated with a very high inverse wave age peak $1/\beta = 1.5$. In this situation, the difference between magnitudes of $\boldsymbol{\tau}_{\mathbf{a}}$ and $\boldsymbol{\tau}_{\mathbf{oc}}$ reaches 0.4 N/m^2, and the ratio Ra increases to 21%.

In this section, surface wave effects on WPI and NI-KE are examined, based on the slab model with mixed layer depth specified as H = 50 m, forced by a sudden wind event with the varying momentum fluxes ($\boldsymbol{\tau}_{\mathbf{a}}$ and $\boldsymbol{\tau}_{\mathbf{oc}}$). The two components of the near inertial currents (U, V) of the slab modeled are shown in Figs. 2 (a) and (b). When the effects of the surface waves on the momentum fluxes are not included, both components are overestimated by using the air-side stress $\boldsymbol{\tau}_{\mathbf{a}}$. The largest difference in the near inertial motions occurs during the sudden wind event, up to 13%, which corresponds to the peak event shown in Fig. 1, for both inverse wave age $1/\beta = 1.5$ and also for $\Delta\tau$. After the sudden wind change event, the difference in near inertial currents is generally lower than 5%.

Note that the damping of the near inertial currents takes several inertial periods, or ~ a few days (e.g., Alford 2016). Therefore, after a sudden wind event, strong near inertial currents will last for several days before dissipation, which results from the latitude-dependent damping parameter r in the slab model. The time series of NI-KE_{a} and NI-KE_{oc} calculated from the near inertial currents driven by $\boldsymbol{\tau}_{\mathbf{a}}$ and $\boldsymbol{\tau}_{\mathbf{oc}}$, are shown in Fig. 2(c), and the corresponding time-integrated estimates of NI-KE, in Fig. 2(d). Here, the time-integrations are computed as $\int \text{NI-KE}_{\text{a}} dt$ and $\int \text{NI-KE}_{\text{oc}} dt$ over January 2005. An overestimate (by 35%) occurs in NI-KE_{a} just after the onset of the sudden wind change event in Fig 2(c) because of the overestimates of the near inertial velocity by the air-side wind stress. Moreover, during this wind change event, the difference in the time-integrated values for NI-KE, specifically $\int \text{NI-KE}_{\text{a}} dt$ and $\int \text{NI-KE}_{\text{oc}} dt$, is up to 40%, and is primarily determined by the increase in NI-KE_{a}, as shown in Fig. 2(d). By comparison, during other times (before and after the sudden wind change event), overestimates in the near inertial current only contribute 5% to the total NI-KE difference, due to relatively weak wind variations.

Finally, by considering the combined effects of forcing stresses ($\boldsymbol{\tau}_{\mathbf{a}}$ and $\boldsymbol{\tau}_{\mathbf{oc}}$) and near inertial currents, the time series (denoted Π_{a} and Π_{oc}), and time-integrations of WPIs (denoted as $\int \Pi_{\text{a}} dt \ and \int \Pi_{\text{oc}} dt$.) are given in Fig. 2(e)-2(f). Consistent with above results, the difference between $\int \Pi_{\text{oc}} dt$ and $\int \Pi_{\text{a}} dt$ also reflects the overestimated wind power input (WPI) to the near inertial currents, reaching 19%; most of the contributions from the surface wave effects in Fig. 2(f) occur during the sudden wind change event. By comparison, the damping of near inertial currents is sometimes overestimated by air-side stress $\boldsymbol{\tau}_{\mathbf{a}}$, as indicated by the negative values of

WPI, shown in Fig. 2(e), denoted as π_a and π_{oc}. Here, the relative direction between $\boldsymbol{\tau}_\mathbf{a}$ and the near inertial current is over 90 degrees. Note that although the time series of WPI can have negative values, indicated as π_a and π_{oc} in Fig. 2(e), the time-integrated series for WPI is always positive, indicated as $\int \pi_a dt\ and \int \pi_{oc} dt$ in Fig. 2(f). This suggests that the effects of surface waves will always lower the wind power input to the near inertial motions, particularly those resulting from sudden wind change events, such as storms and moving fronts in mid-latitudes.

Thus, we have found that the momentum flux is sometimes overestimated when surface waves are neglected, based on the single-point numerical experiment for sudden wind change events. In fact, WPI and NI-KE are relatively small and can be neglected even when the sea state corresponds to actively growing waves, with inverse wave age $1/\beta > 0.83$. For example, although $1/\beta$ is around 1 on day 9.2 in Fig. 1, the wind speed is relatively low at 7.2 m/s, and causes a very small negligible overestimate in the magnitudes for WPI and NI-KE, as indicated by Figs. 2(c) and 2(d). Therefore, for surface waves to have large effects on WPI, there must be relatively high values for varying wind speeds (wind stress), and thus, big differences between the magnitudes of $\boldsymbol{\tau}_\mathbf{a}$ and $\boldsymbol{\tau}_\mathbf{oc}$, as well as for the inverse wave ages (young waves).

Therefore, an additional joint parameter μ, denoted as the Wave-Effect-Parameter (WEP) and based on inverse wave age $1/\beta$ and $\Delta\tau$, is defined as

$$\mu = \begin{cases} -\Delta\tau \times \frac{1}{\beta} & \text{if } \Delta\tau < 0 \text{ and } \frac{1}{\beta} < 0 \\ \Delta\tau \times \frac{1}{\beta} & \text{if otherwise} \end{cases} \quad . \qquad (14)$$

We show that the Wave-Effect-Parameter μ is a useful indicator for the effective identification of surface wave effects on WPI. The WPI difference, $\Delta\Pi = \Pi_{\mathbf{a}} - \Pi_{\mathbf{oc}}$, is defined as the difference between the WPIs calculated by $\boldsymbol{\tau}_{\mathbf{a}}$ and by $\boldsymbol{\tau}_{\mathbf{oc}}$. The correlation coefficient *R* between $\Delta\Pi$ and μ is 0.51 as displayed in Fig. 3, for the single-point experiment. For some particular locations in the open ocean, the correlation coefficient *R* may be reduced because of a couple of factors. First, typical hurricane/storm wind events might have shorter durations than NIMs (several days before being dissipated). Second, NIMs are very sensitive to the presence of previous NIMs, generated by previous wind events, which therefore affect WPI and thus, $\Delta\Pi$ and *R*. Both factors may cause variations in $\Delta\Pi$ and μ to occur at different times, thereby resulting in reduced simultaneity and lowered correlation coefficient.

Following the method used for the single-point experiment, but using the climatological monthly mixed layer depth, we calculate the time series for the means of $\Delta\tau$, inverse wave age $1/\beta$, the Wave-Effect-Parameter μ, and the WPI difference $\Delta\Pi$ for the global ocean, the tropics (20°S -20°N), northern mid-latitudes (30°N-65°N and southern mid-latitudes (35°S-65°S), as shown in Fig. 4 (a)-(d). For northern and southern mid-latitude regions, relatively high values of $1/\beta$, μ and $\Delta\tau$ are found, which generally correspond to high $\Delta\Pi$. In these storm track regions, WPI is overestimated significantly when surface wave effects are neglected, which is reflected by $\Delta\pi$, shown in Fig. 4(d). For tropical regions, low values for $1/\beta$, μ and $\Delta\tau$ are found, corresponding to very small values for $\Delta\pi$, which can be negligible. The global mean of $\Delta\pi$ is also quite small, compared to storm track areas. Noting that the conclusions for surface wave effects on WPI from the spatial mean are complicated and not so straightforward as those of the single-point experiments. That is because the NIMs are determined by variations in $\frac{T}{H}$, indicated by equation (7). Thus, spatial variations of mixed layer depth "contaminate" the general conclusion for surface wave effects on WPIs. Therefore, a detailed analysis of geographical distribution $1/\beta$, $\mu, \Delta\pi$, and their relationships is necessary to explore the surface waves effects on WPI, which is given in the following sections.

3. Global distribution and features of wave effects on WPI

Based on the analysis of the previous section, it appears that high wind forcing events, like hurricanes or storms, result in WPI estimates that would be overestimated by calculations that ignore the waves. The strongest near inertial currents and highest values for WPI tend to be caused by such hurricanes and storms, usually occurring along the mid-latitude storm tracks. Over the global oceans, the effects of the surface waves should significantly modulate the amplitude of the near inertial currents, and thus affect WPI values. In order to explore and quantify the extent to which the amplitude of WPI is affected by the impacts of surface waves on the water-side stress $\boldsymbol{\tau}_{\mathbf{oc}}$ geographically, both $\boldsymbol{\tau}_{\mathbf{a}}$ and $\boldsymbol{\tau}_{\mathbf{oc}}$ are used to calculate Π_a and Π_{oc}, based on the slab model constructed in Section 2.

a. **Geographical distribution of $\Delta\Pi$**

The time mean (over years 2005-2008) spatial distributions of Π_a and Π_{oc}, forced by $\boldsymbol{\tau}_{\mathbf{a}}$ and $\boldsymbol{\tau}_{\mathbf{oc}}$, respectively, calculated by the slab model gives very similar results (not shown) as presented by previous researchers (*e.g.*, Alford 2001; 2003). The largest wind power input, WPI, occurs around 30°- 50° in the Northern Hemisphere winter, with broad maxima, closely associated with winter storm track regions. Moreover, broad minima span the central and eastern portions of each basin. As a whole, the 4-year average wind power input Π_a by $\boldsymbol{\tau}_{\mathbf{a}}$ is 0.27 TW, which is overestimated by up to 10.3% for the global mean, when the effects of growing waves on the wind momentum flux from atmosphere to near inertial motions are not considered.

On one hand, as demonstrated by Fig. 5, the effect of waves is to reduce the wind power input to near inertial motions in the mixed layer, over the mid-latitude western portions of the Atlantic and Pacific Oceans. These areas provide over two-thirds of the total reduction of WPI. The remaining one-third of the wave-related reductions occurs mainly within the band of 35°- 50°S. On the other hand, negative values of $\Delta\Pi$ can appear over the tropical areas, for example, especially in the east-southern Pacific Ocean. The contributions of these negative values to the total $\Delta\Pi$ are rather negligible (less than 5%), mainly caused by the modulation of the momentum flux with $|\boldsymbol{\tau}_\mathbf{a}| < |\boldsymbol{\tau}_\mathbf{oc}|$ due to swell.

Since most of the wind power input is caused by moving storms which occur in winter time, we consider the effects of surface waves on $\Delta\Pi$ during winter time in both hemispheres. Fig. 5 shows the average $\Delta\Pi$ for winter, which is December, January, and February (DJF) in the North, and June, July and August (JJA) in the South. Thus, the difference occurs mainly over the mid-latitude northwestern Atlantic and Pacific, and the mid-latitude Southern Ocean. There are some exceptions, like large WPI values found in summers over the Gulf of Mexico, due to strong tropical cyclones. Generally, in winters, overestimates in WPI caused by surface waves reach 25% over the storm track areas of the mid-latitude North Atlantic, with a global mean of 11%. In summers, the surface wave effects on $\Delta\Pi$ are not as significant, causing a mean reduction of WPI by about 6% (~0.013 TW, from 0.22 TW to 0.233 TW), globally. Furthermore, as shown in Fig. 5(b), there are negative $\Delta\Pi$ values on both sides of tropics. These areas are mainly dominated by swell and partially mixed sea states. The detailed spatial relationships among $\Delta\Pi$, $1/\beta$, and μ are discussed in the following section.

b. **Relationship between global maps of evolving surface waves and $\Delta\Pi$**

In this section, we investigate the effects of surface waves on WPI as characterized by relationships among $1/\beta$, μ and $\Delta\Pi$. Here, μ and $\Delta\Pi$ are calculated globally following the method used for the single-point experiment in section 2.4. For winter and summer of 4-year time mean, the inverse wave age $1/\beta$, is computed using equation (13) and displayed in Figs. 6(a) and 6(b).

Typically, higher values for the inverse wave age ($1/\beta$ >0.83) correspond to waves that are more strongly coupled to the wind (i.e., transfer of momentum from the wind to waves is larger). Thus, relatively more energy and momentum are stored in the young surface waves than in swell-dominated seas. Under such circumstances, the surface waves will reduce the momentum flux to NIMs and thus reduce the WPI. As demonstrated by Fig. 5, there are mainly two zonal bands at mid-latitudes over both hemispheres, where the effect of waves on WPI is largest, and dominates the $\Delta\Pi$**.** However, as indicated by the averaged inverse wave age distribution shown in Fig. 6, there are three zonal bands in the open oceans with relatively high values for inverse wave age: the mid-latitude storm tracks and the trade wind regions in the North Pacific and North Atlantic, and mid-latitude Southern Ocean. Low values of inverse wave age appear for the eastern portion of the tropics and subtropics, coinciding with areas of relatively minimal wind speeds.

Comparing Figs. 5 and 6, the largest values for $\Delta\Pi$ and inverse wave age (young waves) correspond to the mid-latitude storm track areas, where the wind speeds are highest and change rapidly with more momentum stored in the surface waves, compared to swell-dominated areas with lower winds. Moreover, we find that the lowest values for inverse wave age and even negative $\Delta\Pi$ values occur for swell dominated regions like the eastern Pacific Ocean, where $|\boldsymbol{\tau}_{\mathbf{a}}|$ is equal or less than $|\boldsymbol{\tau}_{\mathbf{oc}}|$. In these regions, surface waves release energy to the atmosphere, transferring wave momentum to the wind (Hanley et al. 2010; Sullivan and McWilliams 2010).

Trade wind regions over the western portion of the North Pacific and North Atlantic Oceans correspond to relatively high inverse wave age, with mostly low values for $\Delta\pi$. The main reason for this situation is that the winds in the trade wind regions are much weaker than those in the mid-latitude storm track areas and thus weaker NIMs are generated. The distributions of air-side stress $|\boldsymbol{\tau}_{\mathbf{a}}|$ for winter and summer are shown in Fig. 7(a) and 7(b). On average, over mid-latitude Pacific and Atlantic regions, and mid-latitude Southern Ocean, $|\boldsymbol{\tau}_{\mathbf{a}}|$ reaches up to 0.3 N/m^2, which is more than three times that of $|\boldsymbol{\tau}_{\mathbf{a}}|$ in the lower latitude trade wind regions. This agrees well with the conclusions of the single-point numerical experiment, that the high winds developed by hurricanes and storms are prerequisites for the importance of evolving surface waves on WPI. Moreover, it is easy to exclude these trade wind regions, where surface waves do not significantly affect WPI, by calculating the Wave-Effect-Parameter μ with equation (14) based on wind stress and inverse wave age. As shown by Fig. 7(c) and 7(d), μ is very low in these regions, with even negative values in the tropics, as determined by values for $\Delta\tau$ or $1/\beta$.

Note that there are two regions with very high values for $1/\beta$ and μ, corresponding to low values for $\Delta\pi$: i) Coastal or closed/semi-closed regions, where fetch effects cause high $1/\beta$ and thus high μ, like Taiwan Strait and coastal areas of the Mediterranean Sea. ii) High latitudes > 55° for both hemispheres, where both $1/\beta$ and wind speed are high and thus μ and $\Delta\tau$ are high. The main reason for this result is that the joint effect of a deep mixed layer depth and reduced near inertial variability of the wind causes much weaker inertial currents and thus much lower values for WPI and $\Delta\Pi$ than those that are obtained in areas of the mid-latitude storm tracks.

The inverse wave age values presented in Fig. 6 are averaged over 4 years, which means that it is possible to identify the regions that are dominated by wind sea or swell regimes, but not possible to identify how frequently these regimes occur. Moreover, the peaks in the inverse wave age, which generally correspond to large values for $\Delta\Pi$ occurring in the open ocean**,** are significantly smoothed. In addition, the generation of strong NIMs depends on highly intermittent wind events, which can cause peaks in resulting inverse wave age values.

In order to understand the frequency of occurrence for the lowering of the WPI by surface wave effects, a technique following Hanley et al. (2010) is used. The frequency of occurrence, is defined as 1 if the inverse wave age is $1/\beta$ >0.83 for wind wave regimes and 0 otherwise. Taking an average of the frequency of occurrence provides the fraction of the time that the ocean is in the wind wave regime. Corresponding to the swell–dominated regime, the frequency of occurrence is also defined to be 1 if the inverse wave age is $1/\beta$ <0.15 and 0 otherwise. Figures 8(a) and 8(b) show the frequency of occurrence of the wind sea regime for winter and summer time, averaged over 2005-2008; these results lead to estimates for the fraction of time that the ocean is in the wind sea regime or the swell regime, in Figs. 8(c) and 8(d). Growing waves are commonly exhibited in Figs. 8(a) and 8(b) over the mid-latitude storm track areas. It is found that in both winters and summers, growing young waves are dominant less than 10% of the total time, contributing to nearly the total reduction of WPI (e.g. most of $\Delta\pi$).

These results confirm that the wave effects on WPI are intermittent, consistent with the peaks in the inverse wave age distributions and the largest values for $\Delta\pi$ occurring in the mid-latitude storm track areas. Moreover, as shown in Figs. 8(c) and 8(d), swell dominates the eastern side of the Indian, Pacific, and Atlantic Oceans, corresponding to the three swell pools identified by Chen et al. (2002). It appears that during either winters or summers, the average frequency of occurrence for swell can reach 70%. Moreover, wind speeds and the Wave-Effect-Parameter μ values (indicating the importance of surface waves on WPI) in these regions are much weaker than those of the mid-latitudes. Therefore, surface waves are in near-equilibrium and the effects of evolving surface waves on WPI are negligible.

We show additional confirmation of the influence of evolving surface waves on WPI and $\Delta\pi$ in Figs. 9(a)–(f): zonal means of $\Delta\pi$, air-side stress $|\boldsymbol{\tau}_{\mathbf{a}}|$, μ, frequency of occurrence of wind sea and swell regimes and inverse wave age. The zonal mean for $\Delta\pi$ shows that the effects of growing surface waves are dominant on WPI in winters over the storm track regions. The blue line has two peaks over mid-latitude storm track areas in both hemispheres, centered at about 40°N and 45°S (Fig. 9(a)). These peaks correspond to relatively high μ and frequencies of concurrency for wind sea (10%), as shown in Fig. 9(c) and (d). In tropical regions, the effects of surface waves on $\Delta\pi$ are weak for both summer and winter seasons. Tropical regions correspond to relative high frequencies of concurrency for swell, and low values for air side stress and μ, as shown in Fig. 9(e), (b) and (c). At about 15°N in the trade winds region, there are relatively high values for the frequency of concurrency (~about 10% Fig. 9(d)) and inverse wave age (Fig. 9(f)) for winter. However, the trade wind region corresponds to a weak wind stress, indicated by the blue line in Fig. 9 (b). Thus, μ is low as shown in Fig. 9(c). On one hand, at high latitudes, the mixed layer is very deep and the near inertial currents are inversely proportional to the mixed layer depth. On the other hand, there is a reduction in the near inertial wind variability (Rath et al. 2014). Both factors cause relative weak generation of near inertial currents, and therefore small values for WPI and $\Delta\pi$, along with high values for air-side wind stress, μ and frequency of concurrency for wind sea, shown in Fig. 9 (a)-(d).

4. Conclusions and discussions

In the present study, we quantify the influence of evolving surface waves on WPI through using momentum fluxes from a spectral wave model: air-side stress $\boldsymbol{\tau}_{\mathbf{a}}$ and water-side stress $\boldsymbol{\tau}_{\mathbf{oc}}$. The surface wave effects on WPI are analyzed by using a single-point numerical experiment, as well as by a global ocean time mean analysis.

For a sudden wind change event, the single-point numerical experiment shows that when surface wave effects on momentum flux are not considered, overestimates are 20% for WPI and 40% for NI-KE. Over the open oceans, we conclude the following:

1) Without considering the surface wave effects, the 2005-2008 global time mean WPI is overestimated by a non-negligible 10%. In the winter seasons the WPI overestimates due to the neglect of surface waves reaches 25%, over storm track areas of the North Atlantic, with a global mean of 12%. In the summer seasons, the surface wave effects on the WPI difference $\Delta\Pi$**,** are not as significant, causing a mean reduction in WPI of about 6% over the entire ocean.

2) Two regions where the reductions in WPI due to surface waves are maximal are determined. One is the mid-latitude northwestern portions of the Atlantic and Pacific Oceans, contributing over two thirds of the total reduction of WPI. A second region is the band between 35°S and 50°S, over the winter storm track regions of the Southern Ocean, which contributes to remaining one third reduction of WPI. Although some areas of negative values for $\Delta\Pi$ can appear over the tropical areas over the east-southern Pacific and Atlantic Oceans, their contributions to the total $\Delta\Pi$ appear to be negligible.

3) We analyzed the relationships between inverse wave age $1/\beta$, the Wave-Effect-Parameter μ, and $\Delta\Pi$ in geographical space and calculated zonal means. It is found that hurricanes and storms are prerequisites for situations where surface waves are important contributors to WPI, generally with high values for

$1/\beta$ and μ. However, there are exceptions. For high latitudes and some enclosed, or semi-enclosed regions, although values for $1/\beta$ and μ are high, results suggest that corresponding values for $\Delta\pi$ are low and consequently the impacts of surface waves are small.

4) Relatively low frequencies of occurrence of wind sea are found in the mid-latitudes. This implies that the influence of evolving surface waves on WPI is intermittent, occurring less than 10% of the total time, but making up the dominant contributions to overestimates in WPI.

Estimates of WPI have been extensively investigated over the last decade (e.g., Alford 2001). However, these estimates overlooked the effects of surface wave on momentum fluxes. As shown in the present study, WPI is reduced because of the effects of surface wave effects. Our results point to the potential role of surface wave effects in influencing the upper and interior ocean processes by modulating the NIMs. Specifically, for the upper ocean, growing surface waves absorb and store wind momentum and energy, thereby lowering the intensity of NIMs and thus, their shears at the base of the mixed layer. Consequently, less vertical mixing occurs in the upper ocean, resulting in relatively higher sea surface temperatures, which is crucial to every aspect of upper ocean dynamics, such as for heat flux exchanges under tropical cyclones (e.g., Chen and Curcic 2016).

For the interior ocean, NIWs are capable of propagating downward and equatorward into the deep ocean, interacting with the rest of the internal wave continuum (Henyey et al. 1986) and thus causing mixing in the abyssal oceans. Therefore, a lowered WPI because of surface wave effects might induce weaker diapycnal mixing and meridional overturning circulation, which are key processes for climate variation. Specifically, since estimates for WPI are reduced by 20% by considering the ocean-surface-velocity dependent wind stress parameterization (Rath et al. 2013), together with about 10% reduction caused by surface wave effects, there is a one-third reduction in WPI, compared to previous estimates. Typically, only around 20% of the WPI can penetrate into the deep ocean (Furuichi et al. 2008; Zhai et al. 2009), or even less, ~10% according to Rimac et al (2016). Therefore, it seems that the NIWs might not be as important as previously thought for deep ocean diapycnal mixing, and thus for ocean general circulation (Wunsch and Ferrari 2004).

Our results show the necessity to include the effects of surface wave in estimating WPI in investigating upper ocean processes. However, to date, nearly all climate models and atmosphere-ocean coupled models ignore this physics. Specifically, the coupled atmosphere-ocean models often assume $\boldsymbol{\tau}_{\mathbf{a}} = \boldsymbol{\tau}_{\mathbf{oc}}$ for the boundary condition at the air-sea interface. Although this appears to be mathematically acceptable and ensures momentum conservation between the atmosphere and ocean systems, it ignores the existence of surface waves and their evolution. Moreover, this approach introduces errors in estimates for the momentum flux from the atmosphere to the ocean, and in estimates for NIMs. The amount of wave momentum that leaves a given hurricane/storm is exactly the excess amount that is delivered to upper ocean currents in a typical atmosphere-ocean coupled model. Basically, surface waves provide the dynamical surface boundary condition that is in perpetual adjustment in response to surface winds and currents. Therefore, surface waves are necessary in accounting for the upper oceanic dynamical processes and the effects of surface waves on the momentum flux and should therefore be included in coupled models. Moreover, as one of the strongest components of surface currents in the open ocean, near inertial currents have an obvious effect on the surface wave heights (up to 20%). This is especially evident at high latitudes, as found in the Northwest Pacific, based on wave buoy records (Gemmrich and Garrett, 2012) and wave-current coupled simulations in the Northeast Atlantic (Liu et al., 2015). The detailed effects of near inertial currents on surface waves will be discussed elsewhere.

Acknowledgments

We are grateful for useful suggestion about the slab model with Matthew H Alford at Scripps Institution of Oceanography and for the momentum flux data provided by Fabrice Ardhuin and colleagues at IFREMER. The corresponding data description can be found at: http://wwz.ifremer.fr/iowaga/Products/WAVEWATCH-III.This study was supported by National Natural Science Foundation of China under Grant: 41506028, Natural Science Foundation of Jiangsu Province under Grant: BK20150913, The National Key Research and Development Program of China: 2016YFC1401407, National Programme on Global Change and Air-Sea Interaction under Grant: GASI-IPOVAI-04, The Startup Foundation for Introducing Talent of NUIST, Canada's Program on Energy Research and Development, Canadian Space Agency's GRIP, Marine Environmental Observation Prediction and Response (MEOPAR), the Canada-Surface Water and Ocean Topography mission (C-SWOT), and the Canadian Aquatic Climate Change Adaptation Services Program.

References

Ardhuin, F., B. Chapron, and T. Elfouhaily, 2004: Waves and the air–sea momentum budget: Implications for ocean circulation modeling. *J. Phys. Oceanogr.*, **34**, 1741–1755.

Ardhuin, F. and A. D. Jenkins, 2006: On the interaction of surface waves and upper ocean turbulence. *J. Phys. Oceanogr*., **36**, 551–557.

Ardhuin, F., E. Rogers, A.V. Babanin, J.-F. Filipot, R. Magne, A. Roland, A. van der Westhuysen, P. Queffeulou, J.-M. Lefevre, L. Aouf, and F. Collard, 2010: Semiempirical dissipation source functions for ocean waves. Part I: definition, calibration, and validation. *J. Phys. Oceanogr*., **40**, 1917–1941.

Alford, M. H., J. A. MacKinnon, H. L. Simmons, and J. D. Nash, 2016: Near-inertial internal gravity waves in the ocean, *Annu. Rev. Fluid Mech.*, **8 (1)**, 150902153948, 007, doi: 10.1146/annurevmarine-010814-015746.

Alford, M. H., 2001: Internal swell generation: the spatial distribution of energy flux from the wind to mixed-layer near-inertial motions. *J. Phys. Oceanogr*.,**31**, 2359–2368.

Alford, M. H., 2003: Improved global maps and 54-years history of wind-work on ocean inertial motions. *Geophys. Res. Lett*., **30**, 1424, doi:10.1029/2002GL016614.

Alford, M. H., and M. Whitmont, 2007: Seasonal and spatial variability of near-inertial kinetic energy from historical moored velocity records. *J. Phys. Oceanogr*. **37**, 2022–2037.

Alves, J. H., M. L. Banner, and I. R. Young, 2003: Revisiting the Pierson–Moskowitz asymptotic limits for fully developed wind waves. *J. Phys. Oceanogr*., **33**, 1301–1323.

Belcher, S. and J. Hunt, 1993: Turbulent shear flow over slowly moving waves. *J. Fluid Mech.*, **251**, 109–148.

Breivik, Ø., K. Mogensen, J-R Bidlot, M. Alonso Balmaseda, and P. A.E.M. Janssen, 2015: Surface wave effects in the NEMO ocean model: forced and coupled experiments. *J. Geophys. Res.*, **120 (4)**, Doi:10.1002/2014JC010565.

Chen, G., B. Chapron, R. Ezraty, and D. Vandemark, 2002: A global view of swell and wind sea climate in the ocean by satellite altimeter and scatterometer. *J. Atmos. Oceanic Technol.*, **19**, 1849–1859.

Chen, S. S. and M. Curcic, 2016: Ocean surface waves in hurricane Ike (2008) and superstorm Sandy (2012): coupled model predictions and observations. *Ocean Modell.*, **103(2007)**, 161–176.

Craig, P. D., and M. L. Banner, 1994: Modeling wave-enhanced turbulence in the ocean surface layer. *J. Phys. Oceanogr.*, **24**, 2546–2559

Craig, P. D., 1996: Velocity profiles and surface roughness under breaking waves. *J. Geophys. Res.*, **101**, 1265–1277.

Crawford, G. B., and W. G. Large, 1996: A numerical investigation of resonant inertial response of the ocean to wind forcing. *J. Phys. Oceanogr.*, **26**, 873–891.

D'Asaro, E. A., 1985: The energy flux from the wind to near-inertial motions in the mixed layer. *J. Phys. Oceanogr.*, **15**, 943–959.

D’Asaro, E. A., C. E. Eriksen, M. D. Levine, P. Niiler, C. A. Paulson, and P. V. Meurs, 1995: Upper-ocean inertial currents forced by a strong storm. Part I: Data and comparisons with linear theory. *J. Phys. Oceanogr*., **25**, 2909–2936.

Dobson, F.W., 1971: Measurements of atmospheric pressure on wind-generated sea waves, *J. Fluid Mech.*, **48**, 91-127.

Donelan, M. A., F.W. Dobson, S. D. Smith, and R. J. Anderson, 1993: On the dependence of sea-surface roughness on wave development. *J. Phys. Oceanogr*., **23**, 2143–2149.

Donelan, M. A., F. W. Dobson, S. D. Smith and R. J. Anderson, 1995: "Reply", *J. Phys. Oceanogr*., **25(8)**, 1908-1909.

Donelan, M. A., 1998: Air-water exchange processes, in Physical Processes in Lakes and Oceans, *Coastal Estuarine Stud*., vol. 54, edited by J. Imberger, 19–36, AGU, Washington, D. C.

Drennan, W. M., H. C. Graber, D. Hauser, and C. Quentin, 2003: On the wave age dependence of wind stress over pure wind seas. *J. Geophys. Res*., **108**, 8062, doi:10.1029/2000JC000715.

Fan, Y., I. Ginis, and T. Hara, 2010: Momentum flux budget across the air-sea interface under uniform and tropical cyclone winds. *J. Phys. Oceanogr*., **40**, 2221–2242.

Fan, Y., and S. M. Griffies, June 2014: Impacts of parameterized Langmuir turbulence and non-breaking wave mixing in global climate simulations. *J. Climate*, **27(12)**, DOI:10.1175/JCLI-D-13-00583.1 .

Ferrari, R. and C. Wunsch, 2009: Ocean Circulation Kinetic Energy: Reservoirs, Sources and Sinks, *Ann. Rev. Fluid Mech.*, **41**, 253-282

Furuichi, N., T. Hibiya, and Y. Niwa, 2008: Model-predicted distribution of wind-induced internal wave energy in the world's oceans. *J. Geophys. Res*., **113**, C09034, doi: 10.1029/ 2008JC004768.

Gemmrich J. and C. Garrett, 2012: The Signature of Inertial and Tidal Currents in Offshore Wave Records, *J. Phys. Oceanogr*., **42**, 1051-1056.

Hanley, K. E., S. E. Belcher, and P. P. Sullivan, 2010: A global climatology of wind–wave interaction. *J. Phys. Oceanogr*., **40**, 1263–1282.

Hasselmann, K., 1970: Wave-driven inertial oscillations. *Geophys. Fluid Dyn*., **1**, 463–502.

Hasselmann, K., T. P. Barnett, E. Bouws, H. Carlson, D. E. Cartwright, K. Enke, J. A. Ewing, H. Gienapp, D. E. Hasselmann, P. Krusemann, A. Meerburg, P. Müller, D. J. Olbers, K. Richter, W. Sell and H. Walden. 1973: Measurements of wind-wave growth and swell decay during the joint North Sea wave project (JONSWAP). *Dtsch. Hydrogr. Zeitschrift.*

Henyey, F. S., J. Wright, and S. M. Flatté, 1986: Energy and action flow through the internal wave field. *J. Geophys. Res*, **91,** 8487–8495.

Holthuijsen, L. H., 2007: Waves in Oceanic and Coastal Waters. Cambridge University Press, 387 pp.

Hwang, P. A., 2016: Fetch- and duration-limited nature of surface wave growth inside tropical cyclones: With applications to air-sea exchange and remote sensing. *J. Phys. Oceanogr.*, **46**, 41-56, doi: 10.1175/JPO-D-150173.1.

Janssen, P. A. E. M., 2004: The interaction of ocean waves and wind, Cambridge University Press, Cambridge, 300 pp.

Janssen, P. A. E. M., 2012: Ocean wave effects on the daily cycle in SST, *J. Geophys. Res.*, **117**, C00J32, doi: 10.1029/2012JC007943, 2012.

Jiang, J., Y. Liu, and W. Perrie, 2005: Estimating the energy flux from the wind to ocean inertial motions: The sensitivity to surface wind fields. *Geophys. Res. Lett.*, **32**, L15610, doi: 10.1029/2005GL023289.

Jing. Z., and L. Wu, 2014: Intensified diapycnal mixing in the midlatitude western boundary current. *Sci. Rep.*, **4**, 7412, doi: 10.1038/srep07412.

Jing. Z., Lixin Wu and Xiaohui Ma, 2015: Improve the simulations of near-inertial internal waves in the ocean general circulation models, *J. Atmos. Oceanic Technol.*, **32**, 1960–1970.

Jing. Z., Lixin Wu and Xiaohui Ma, 2016: Sensitivity of near-inertial internal waves to spatial interpolations of wind stress in ocean generation circulation models. *Ocean Modell.*, **99**, 15-21.

Jochum, M., B. P. Briegleb, G. Danabasoglu, W. G. Large, N. J. Norton, S. R. Jayne, M. H. and F. O. Bryan 2013: The impact of oceanic near-inertial waves on climate, *J. Climate*., **26(9)**, 2833–2844

Klein Patrice, Lapeyre Guillaume, Large W, 2004: Wind ringing of the ocean in presence of mesoscale eddies. *Geophys. Res. Lett.*, **31(15),** 1-4.

Komen, G. J., L. Cavaleri, M. Donelan, K. Hasselmann, S. Hasselmann, and P. A. E. M. Janssen, 2004: Dynamics and Modelling of Ocean Waves, 532 pp., Cambridge Univ. Press, New York.

Kunze, E. 1985: Near-inertial wave propagation in geostrophic shear, *J. Phys. Oceanogr*., **15**, 544 – 565.

Liu, G., Y. He, H. Shen and J. Guo, 2011: Global drag coefficient estimates from scatterometer wind and wave steepness, *IEEE Trans. Geosci. Remote Sens*., **49(5)**, 1499–1503.

Liu, G., and W. Perrie, 2013: Sea-state-dependent wind work on the oceanic general circulation, *Geophys. Res. Lett*., **40**, 3150–3156, doi:10.1002/grl.50624.

Liu, G., and W. Perrie, 2015: Effects of inertial current on the oceanic surface waves: a dataset constructed by matching HF radar current and NDBC buoy records, *7th International Symposium on Gas Transfer at Water Surface*, APL, Seattle, USA, 18-21 May, 2015.

McWilliams, J. C., P. P. Sullivan, and C.-H. Moeng, 1997: Langmuir turbulence in the ocean. *J. Fluid Mech*., **334**, 1–30, doi: 10.1017/S0022112096004375

McWilliams, J. C., J. Restrepo, and E. Lane, 2004: An asymptotic theory for the interaction of waves and currents in coastal waters. *J. Fluid Mech.*, **511**, 135–178, doi:10.1017/S0022112004009358.

McWilliams, J. C., E. Huckle, J.-H. Liang, and P. P. Sullivan, 2012: The wavy Ekman layer: Langmuir circulations, breaking waves, and Reynolds stress. *J. Phys. Oceanogr.*, **42**, 1793–1816.

Miles, J. W., 1957: On the generation of surface waves by shear flows. *J. Fluid Mech.*, **3**, 185-204.

Miles, J. W., 1962: On the generation of surface waves by shear flows. part 4. *J. Fluid Mech.*, **13,** 433–448.

Miles, J.W., 1965: A note on the interaction between surface waves and wind profiles. *J. Fluid Mech.*, **22**, 823-827.

Monterey, G. and S. Levitus 1997: Seasonal variability of mixed layer depth for the world ocean. *NOAA ATLAS*, Nestles, **14**, Washington, D.C., 96 pp.

Munk W. and Wunsch, C., 1998: Abyssal recipes II: energetics of tidal and wind mixing, *Deep-Sea Res. I.*, **45**, 1977–2010.

Perrie, W., and B. J. Toulany, 1990: Fetch relations for wind-generated waves as a function of wind-stress scaling. *J. Phys. Oceanogr.*, **20,** 1666–1681.

Phillips, O. M., 1957: On the generation of waves by turbulent wind. *J. Fluid Mech.*, **2**, 415–417.

Phillips, O. M., 1977: Dynamics of the upper ocean, Cambridge U. Press

Plueddemann, A.J. and J. T. Farrar, 2006: Observations and models of the energy flux from the wind to mixed-layer inertial currents. *Deep Sea Research II*, **53**, 5-30, doi:10.1016/j.dsr2.2005.10.017.

Polton, J. A., and S. E. Belcher, 2007: Langmuir turbulence and deeply penetrating jets in an unstratified mixed layer. *J. Geophys. Res*., **112**, C09020, doi:10.1029/2007JC004205.

Qiao, F., Y. Yuan, Y. Yang, Q. Zheng, C. Xia, and J. Ma, 2004: Wave-induced mixing in the upper ocean: Distribution and application to a global ocean circulation model. *Geophys. Res. Lett*., **31**, L11303, doi:10.1029/2004GL019824.

Rascle, N., F. Ardhuin, and E. A. Terray, 2006: Drift and mixing under the ocean surface. a coherent one-dimensional description with application to unstratified conditions. *J. Geophys. Res*., **111**, C03016, doi: 10.1029/2005JC003004.

Rascle, N., F. Ardhuin, P. Queffeulou, D. Croiz´e-Fillon, 2008: A global wave parameter database for geophysical applications. part 1: wave-current-turbulence interaction parameters for the open ocean based on traditional parameterizations. *Ocean Modell*., **25**, 154–171, doi:10.1016/j.ocemod.2008.07.006.

Rascle, N. and F. Ardhuin, 2013: A global wave parameter database or geophysical applications, Part 2: model validation with improved source term parameterization, *Ocean Modell*., **29**, 2013.

Rath, W., R. J. Greatbatch, and X. Zhai, 2013: Reduction of near-inertial energy through the dependence of wind stress on the ocean-surface velocity, *J. Geophys. Res.*, **118**, 2761-2773, doi:10.1002/jgrc.20198.

Rath, W., R. J. Greatbatch, and X. Zhai, 2014: On the spatial and temporal distribution of near-inertial energy in the Southern Ocean. *J. Geophys. Res.*, **119**, 359–376, doi:10.1002/2013JC009246.

Rimac, A., J. S. von Storch, C. Eden, and H. Haak, 2013: The influence of high-resolution wind stress field on the power input to near-inertial motions in the ocean. *Geophys. Res. Lett.*, **40**, 4882–4886, doi:10.1002/grl.50929.

Rimac, A., J. S. von Storch and C. Eden, 2016: The Total Energy Flux Leaving the Ocean's Mixed Layer. *J. Phys. Oceanogr.*,**46**, 1885-1900.

Saha, S., S. Moorthi, H.-L. Pan, X. Wu, J. Wang, S. Nadiga, P. Tripp, R. Kistler, J. Woollen, D. Behringer, H. Liu, D. Stokes, R. Grumbine, G. Gayno, J. Wang, Y.-T. Hou, H. ya Chuang, H.-M.H. a. J.S. Juang, M. Iredell, R. Treadon, D. Kleist, P.V. Delst, D. Keyser, J. Derber, M. Ek, J. Meng, H. Wei, R. Yang, S. Lord, H. van den Dool, A. Kumar, W. Wang, C. Long, M. Chelliah, Y. Xue, B. Huang, J.-K. Schemm, W. Ebisuzaki, R. Lin, P. Xie, M. Chen, S. Zhou, W. Higgins, C.-Z. Zou, Q. Liu, Y. Chen, Y. Han, L. Cucurull, R.W. Reynolds, G. Rutledge, and M. Goldberg, 2010: The NCEP Climate Forecast System Reanalysis. *Bull. Amer. Meterol. Soc.*, **91**, 1015–1057.

Skyllingstad, E. D., W. D. Smyth, and G. B. Crawford, 2000: Resonant wind driven mixing in the ocean boundary layer. *J. Phys. Oceanogr*., **30**, 1866–1890.

Snyder, R. L., F.W. Dobson, J. A. Elliot and R.B. Long, 1981: Array measurements of atmospheric pressure fluctuations above surface gravity waves, *J. Fluid Mech*., **102**, 1-59.

Sullivan, P. P. and J. C. McWilliams, 2010: Dynamics of winds and currents coupled to surface waves, *Annu. Rev. Fluid Mech*., **42**, 19–42.

Tolman, H. 2009: User manual and system documentation of WAVEWATCH-III version 3.14, Tech. Note 276, NOAA/NWS/NCEP/MMAB, Camp Springs, Md.

Tolman, H. L., 2014: User manual and system documentation of WAVEWATCH III version 4.18 MMAB Contribution No. 316, 311pp. available on http://polar.ncep.noaa.gov/waves/wavewatch/manual.v4.18.pdf.

Wu, L., A. Rutgersson, and E. Sahlee, 2015: Upper-ocean mixing due to surface gravity waves, *J. Geophys. Res.*, **120**, 8210–8228.

Wunsch, C., and R. Ferrari, 2004: Vertical mixing, energy and the general circulation of the oceans. *Ann. Rev. Fluid Mech.*, **36**, 281–314, doi: 10.1146/annurev.fluid.36.050802. 122121.

Zhai, X., R. J. Greatbatch and J. Zhao, 2005: Enhanced vertical propagation of storm-induced near-inertial energy in an eddying ocean channel model, *Geophys. Res. Lett*., **32**, L18602, doi:10.1029/2005GL023643.

Zhai, X., R. J. Greatbatch, and C. Eden, 2007: Spreading of near-inertial energy in a 1/12° model of the North Atlantic Ocean, *Geophys. Res. Lett.*, **34**, L10609, doi:10.1029/2007GL029895.

Zhai, X., R. J. Greatbatch, C. Eden, and T. Hibiya, 2009: On the loss of wind-induced near-inertial energy to turbulent mixing in the upper ocean, *J. Phys. Oceanogr.*, **39**, 3040-3045.

List of Figures

Fig. 1 Red line indicates the magnitude difference $\Delta\tau$ between $\boldsymbol{\tau}_{\mathbf{a}}$ and $\boldsymbol{\tau}_{\mathbf{oc}}$ (Unit: N/m^2). Blue line indicates the inverse wave age. Time series is from the day 8.5 to day 12.5 January 2005. $\mathrm{Ra} = {}^{\Delta\tau}/_{|\boldsymbol{\tau}_{\mathbf{oc}}|} \times 100\%$.

Fig. 2 Slab model simulations of: (a) U and (b) V components of near inertial currents(blue lines indicate without wave effects, red lines indicate with wave effects), (c) time series of NI-KE (blue line for $\text{NI-KE}_{\mathrm{a}}$ and reds line for $\text{NI-KE}_{\mathrm{oc}}$) (d) time-integrated NI-KE, $\int \text{NI-KE}_{\mathrm{a}} dt$ and $\int \text{NI-KE}_{\mathrm{oc}} dt$ (e) time series of WPIs, denoted Π_{a} and Π_{oc}, indicated as blue and red lines, (f) time-integrated WPIs, denoted $\int \Pi_{\mathrm{a}} dt \ and \int \Pi_{\mathrm{oc}} dt$. Blue lines and reds line are indicated for near inertial currents, NI-KE and WPI from slab model with air-side stress $\boldsymbol{\tau}_{\mathbf{a}}$ and water-side stress $\boldsymbol{\tau}_{\mathbf{oc}}$, respectively.

Fig. 3 Blue line represents $\Delta\Pi$ and red line represents the Wave-Effect-Parameter μ of Jan 2005; the correlation coefficient R between $\Delta\Pi$ and μ is 0.51.

Fig. 4 Time series of Jan 2005 for (a) $\Delta\tau$ (unit: N/m^2); (2) inverse wave age; (3) Wave-Effect-Parameter μ; and (4) the WPI difference $\Delta\Pi$ (unit: W/m^2). Red, blue, green and yellow lines indicate mean values for the global, north mid-latitudes, south mid-latitudes and tropical regions, respectively.

Fig.5 Time mean surface wave effects on wind power input (a) global distribution of $\Delta\Pi$ during winter time (DJF), (b) global distribution of $\Delta\Pi$ during summer time (JJA) (Unit: W/m^2).

Fig. 6 Time mean inverse wave age $1/\beta$: (a) global distribution of $1/\beta$ during winter time (DJF), (b) global distribution of $1/\beta$ during summer time (JJA).

Fig. 7 Global maps of magnitude for time mean air-side stress $|\boldsymbol{\tau}_\mathbf{a}|$ and joint parameter μ. (a) distribution of $|\boldsymbol{\tau}_\mathbf{a}|$ during winter (DJF), (b) distribution of $|\boldsymbol{\tau}_\mathbf{a}|$ during summer time (JJA) (Unit: N/m^2), (c) distribution of Wave-Effect-Parameter μ during winter (DJF), and (d) distribution of μ during summer (JJA).

Fig. 8 The frequency of occurrence of wind sea or swell: (a) frequency of occurrence of wind sea during winter (DJF); (b) frequency of occurrence of wind sea during summer (JJA); (c) frequency of occurrence of swell (mature sea) during winter (DJF); (b) frequency of occurrence of swell (mature sea) during summer (JJA) (Unit: $\times$100%).

Fig. 9 Zonal means of: (a) $\Delta\pi$ (Unit: W/m^2), (b) air-side stress $|\boldsymbol{\tau}_\mathbf{a}|$ (Unit: N/m^2), (c) Wave-Effect-Parameter μ, (d) frequency of occurrence of wind sea (Unit: $\times$100%)., (e) frequency of occurrence of swell (Unit: $\times$100%).; (f) inverse wave age $1/\beta$. The blue lines indicate winter, and the red lines indicate summer.

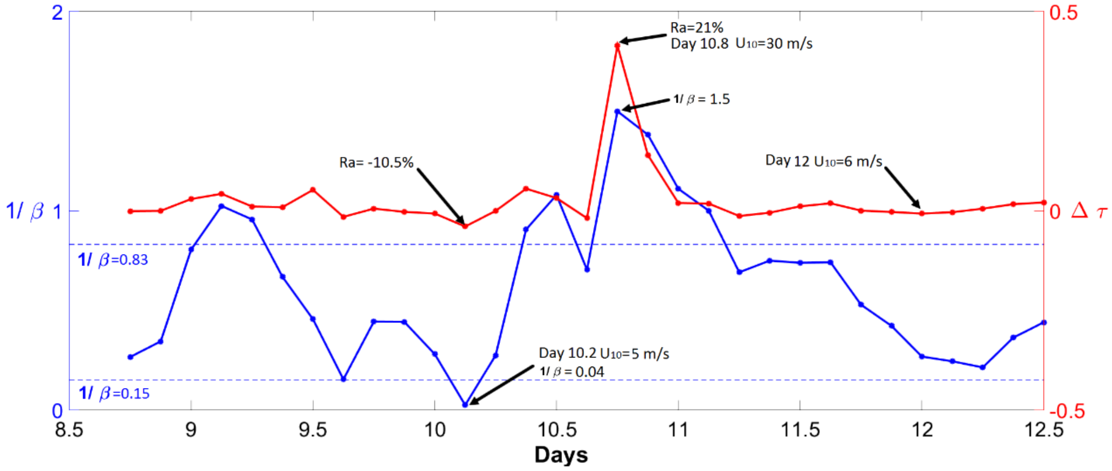

Fig. 1 Red line indicates the magnitude difference $\Delta\tau$ between $\boldsymbol{\tau}_\mathbf{a}$ and $\boldsymbol{\tau}_\mathbf{oc}$ (Unit: N/m^2). Blue line indicates the inverse wave age. Time series is from the day 8.5 to day 12.5 January 2005. Ra $= {}^{\Delta\tau}/_{|\boldsymbol{\tau}_\mathbf{oc}|} \times 100\%$.

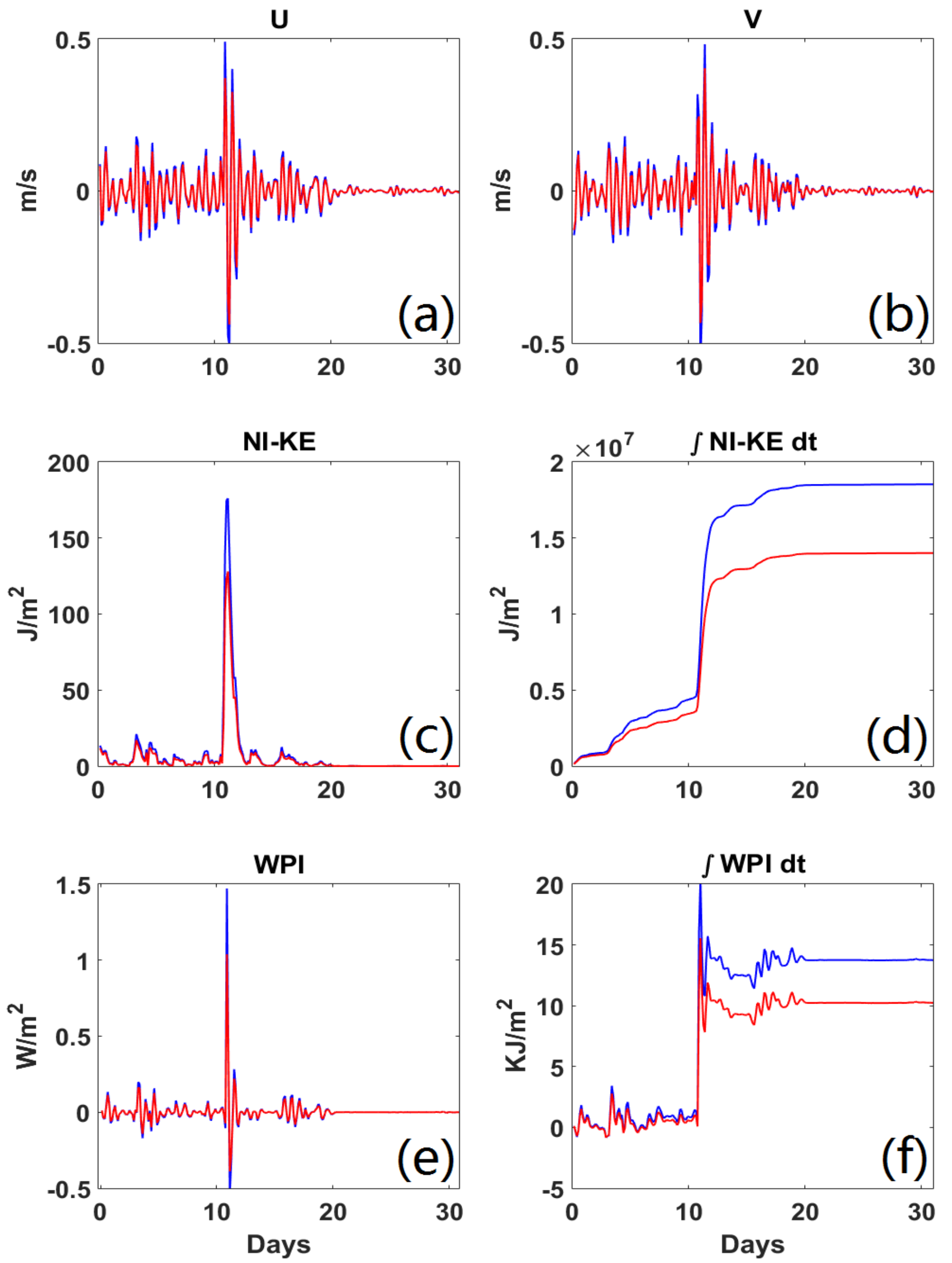

Fig. 2 Slab model simulations of: (a) U and (b) V components of near inertial currents(blue lines indicate without wave effects, red lines indicate with wave effects), (c) time series of NI-KE (blue line for NI-KE_a and red line for NI-KE_oc) (d) time-integrated NI-KE, $\int \text{NI-KE}_\text{a} dt$ and $\int \text{NI-KE}_\text{oc} dt$ (e) time series of WPIs, denoted Π_a and Π_oc, indicated as blue and red lines, (f) time-integrated WPIs, denoted $\int \Pi_\text{a} dt$ *and* $\int \Pi_\text{oc} dt$. Blue lines and red lines are indicated for near inertial currents, NI-KE and WPI from slab model with air-side stress $\boldsymbol{\tau}_\mathbf{a}$ and water-side stress $\boldsymbol{\tau}_\mathbf{oc}$, respectively.

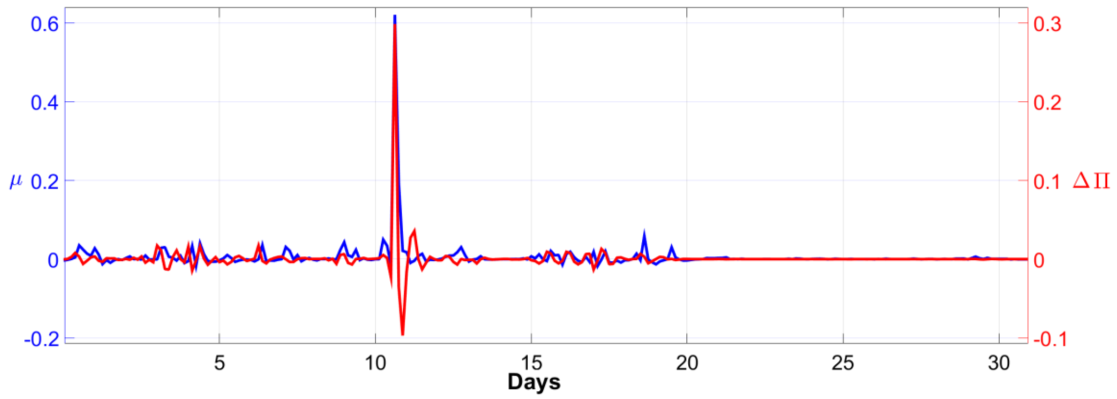

Fig. 3 Blue line represents $\Delta\pi$ and red line represents the Wave-Effect-Parameter μ of Jan 2005; the correlation coefficient R between $\Delta\pi$ and μ is 0.51.

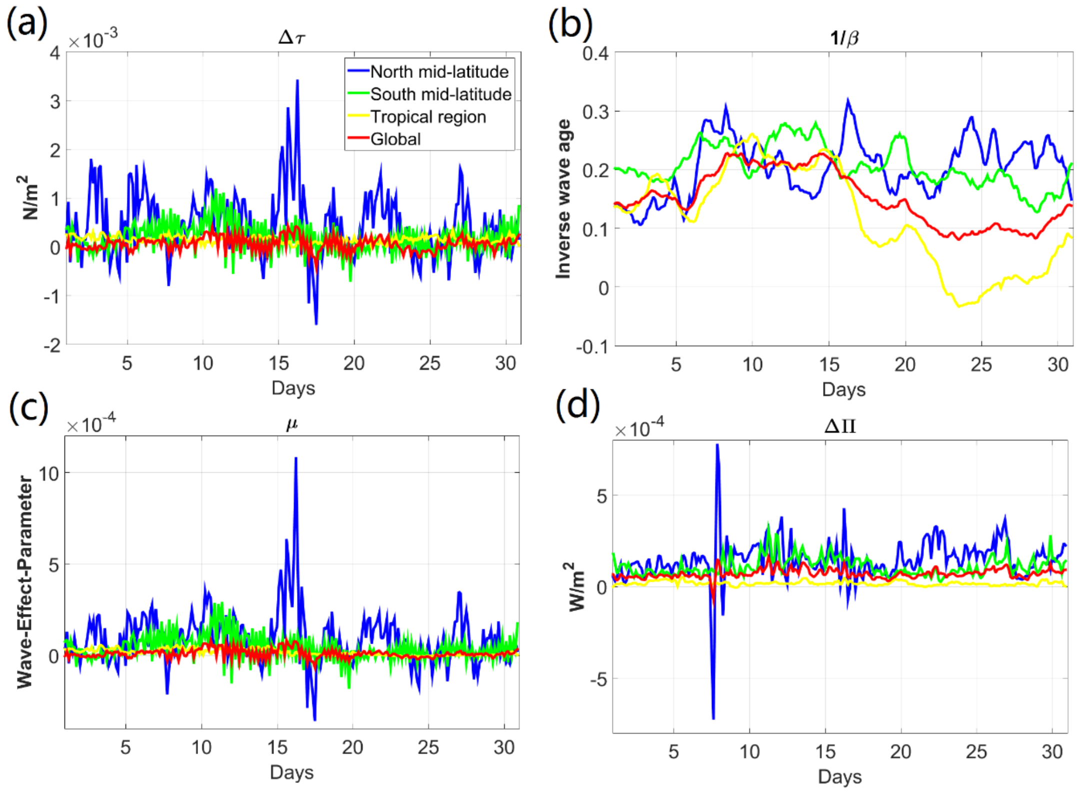

Fig. 4 Time series of Jan 2005 for (a) $\Delta\tau$ (unit: N/m^2); (2) inverse wave age; (3) Wave-Effect-Parameter μ; and (4) the WPI difference $\Delta\pi$ (unit: W/m^2). Red, blue, green and yellow lines indicate mean values for the global, north mid-latitudes, south mid-latitudes and tropical regions, respectively.

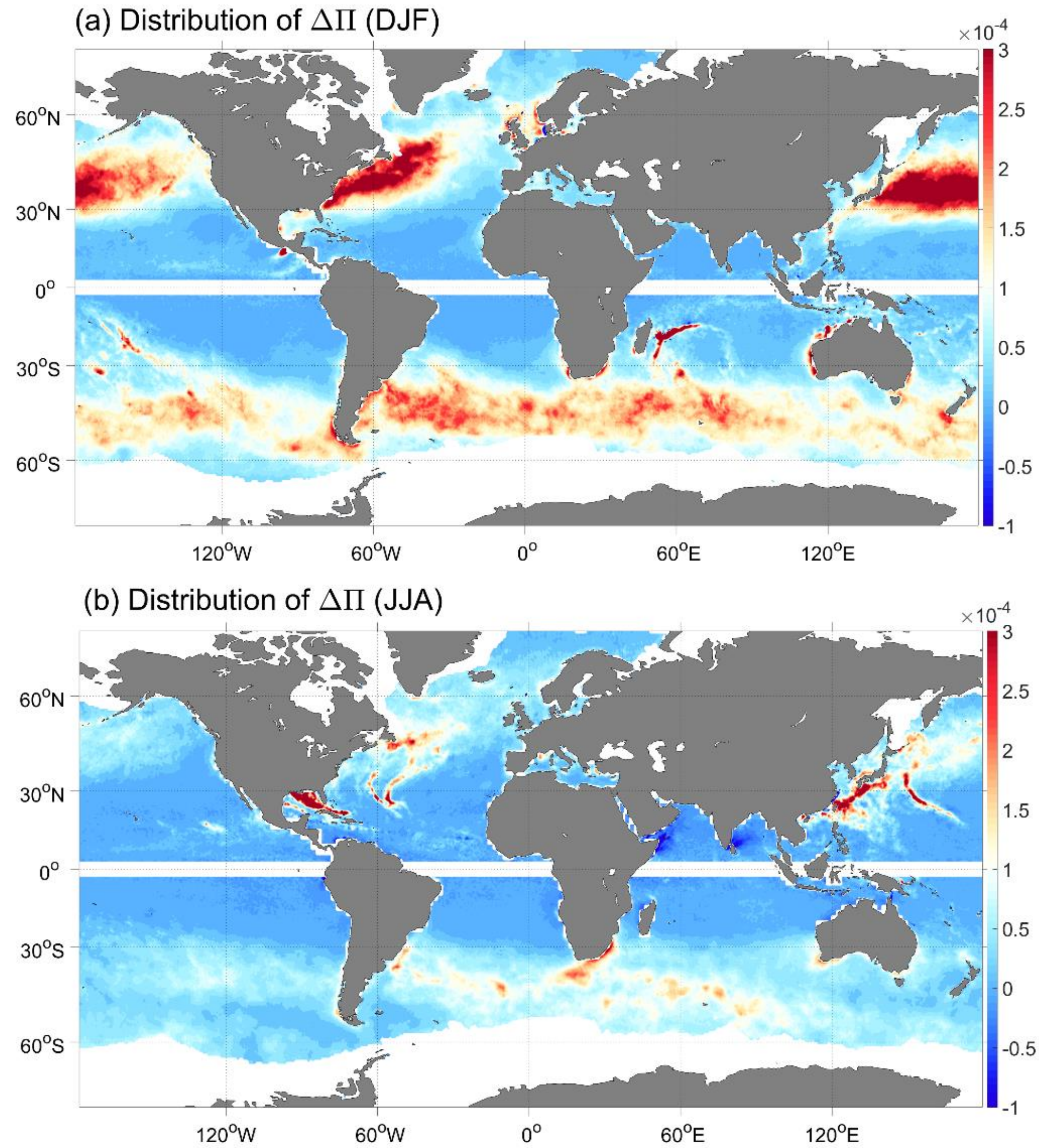

Fig. 5 Time mean surface wave effects on wind power input (a) global distribution of $\Delta\pi$ during winter time (DJF), (b) global distribution of $\Delta\pi$ during summer time (JJA) (Unit: W/m^2).

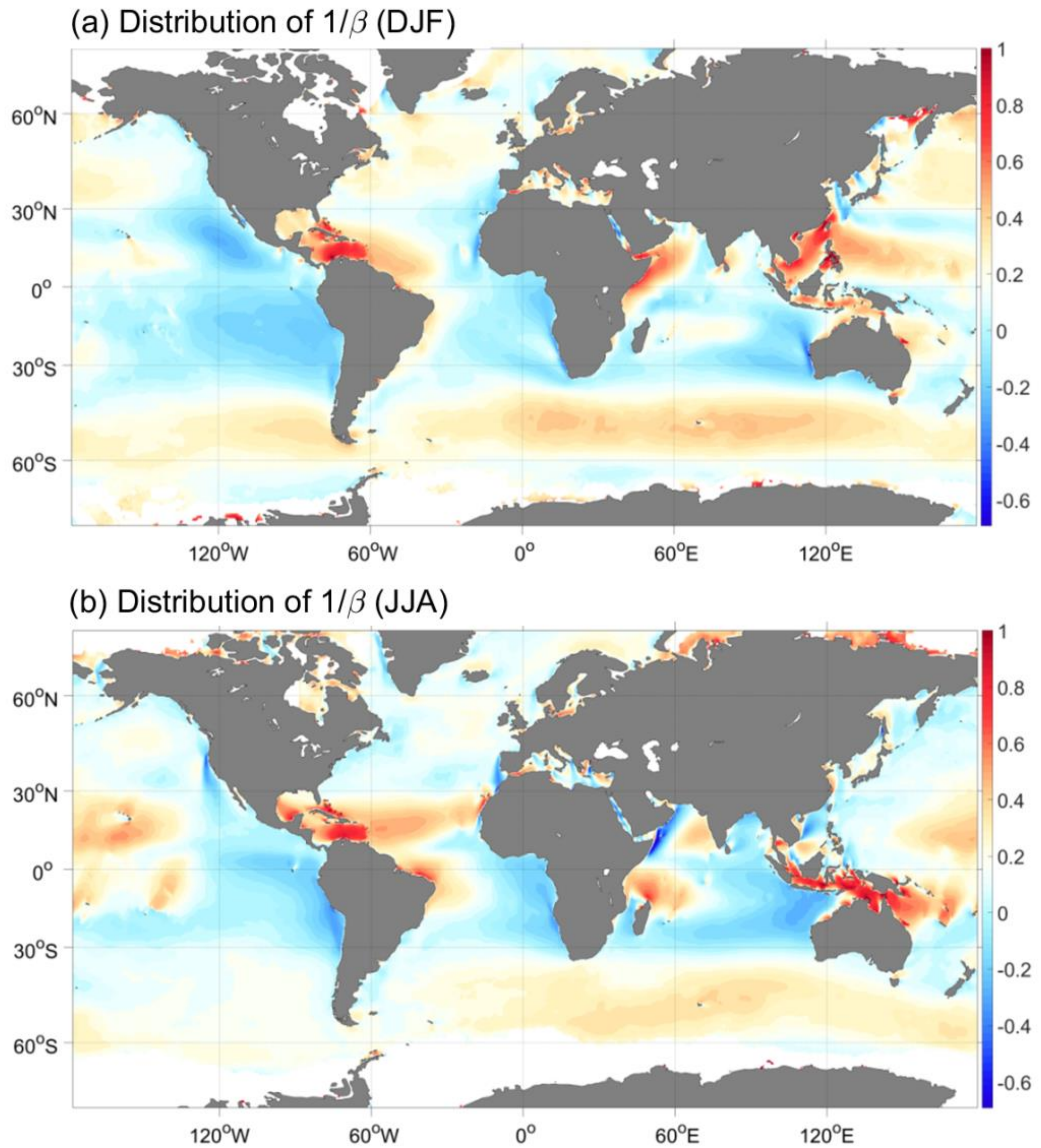

Fig. 6 Time mean inverse wave age $1/\beta$: (a) global distribution of $1/\beta$ during winter time (DJF), (b) global distribution of $1/\beta$ during summer time (JJA).

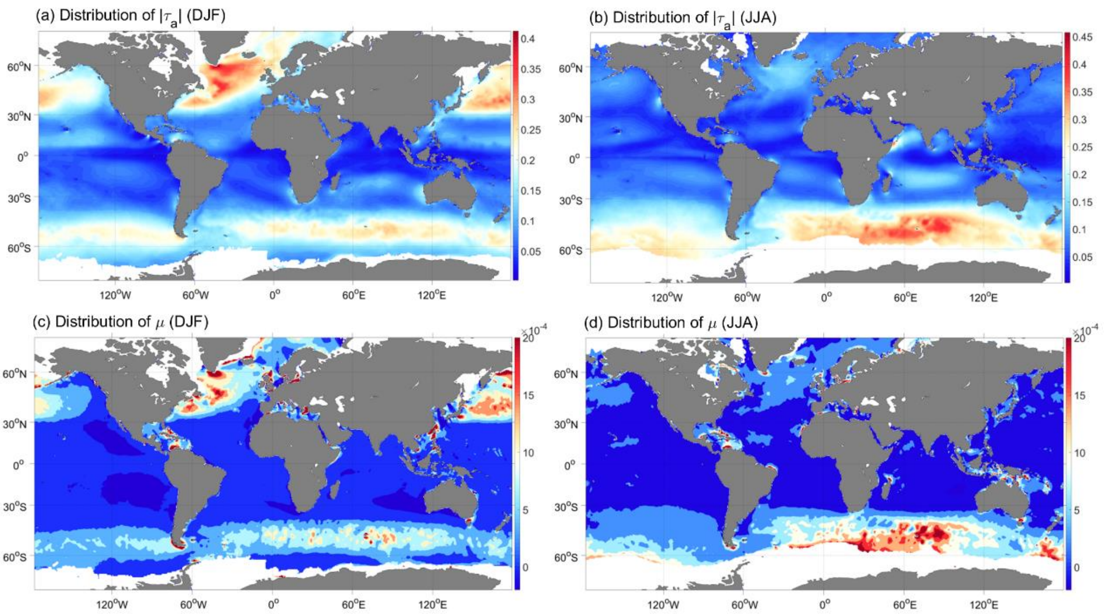

Fig. 7 Global maps of magnitude for time mean air-side stress $|\boldsymbol{\tau}_{\mathbf{a}}|$ and joint parameter μ. (a) distribution of $|\boldsymbol{\tau}_{\mathbf{a}}|$ during winter (DJF), (b) distribution of $|\boldsymbol{\tau}_{\mathbf{a}}|$ during summer time (JJA) (Unit: N/m^2), (c) distribution of Wave-Effect-Parameter μ during winter (DJF), and (d) distribution of μ during summer (JJA).

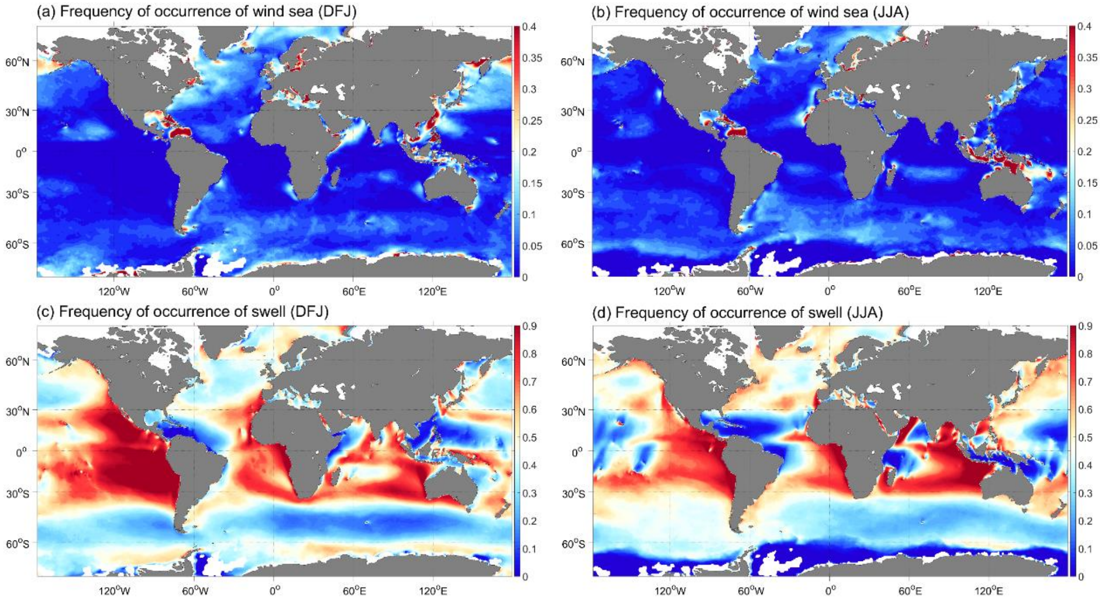

Fig. 8 The frequency of occurrence of wind sea or swell: (a) frequency of occurrence of wind sea during winter (DJF); (b) frequency of occurrence of wind sea during summer (JJA); (c) frequency of occurrence of swell (mature sea) during winter (DJF); (b) frequency of occurrence of swell (mature sea) during summer (JJA) (Unit: ×100%).

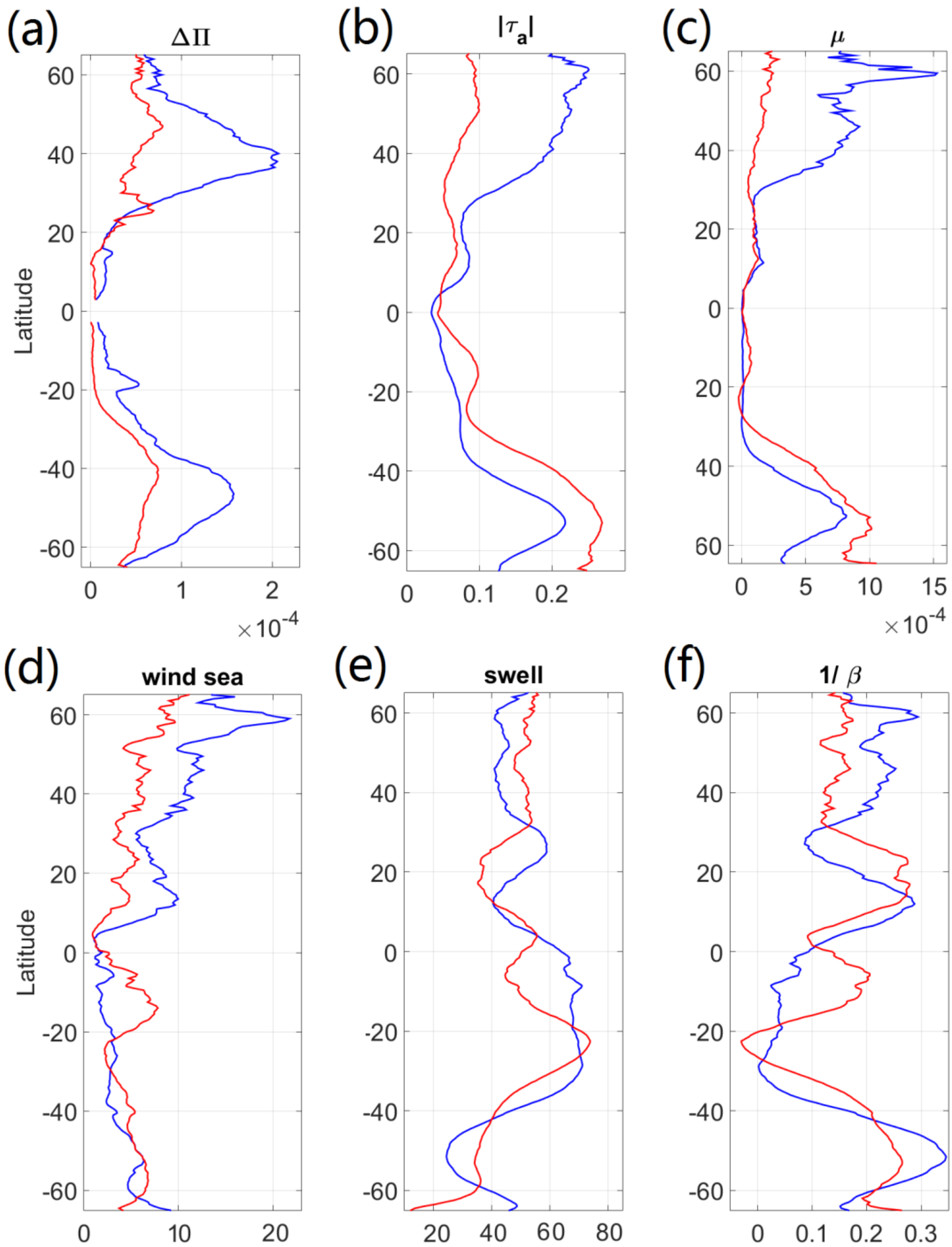

Fig. 9 Zonal means of: (a) $\Delta\pi$ (Unit: W/m^2), (b) air-side stress $|\boldsymbol{\tau}_{\mathbf{a}}|$ (Unit: N/m^2), (c) Wave-Effect-Parameter μ, (d) frequency of occurrence of wind sea (Unit: $\times$100%)., (e) frequency of occurrence of swell (Unit: $\times$100%).; (f) inverse wave age $1/\beta$. The blue lines indicate winter, and the red lines indicate summer.